Dual role of CO in the stability of subnano Pt clusters at the Fe_3O_4(001) surface

Roland Bliem[a], Jessi E. S. van der Hoeven[b], Jan Hulva[a], Jiri Pavelec[a], Oscar Gamba[a], Petra E. de Jongh[b], Michael Schmid[a], Peter Blaha[c], Ulrike Diebold[a], and Gareth S. Parkinson[a,1]

[a]Institute of Applied Physics, TU Wien, 1050 Vienna, Austria; [b]Inorganic Chemistry and Catalysis, Debye Institute for Nanomaterials, Utrecht University, NL-3584 CG Utrecht, The Netherlands; and [c]Institute of Materials Chemistry, TU Wien, 1040 Vienna, Austria

Edited by Thomas E. Mallouk, The Pennsylvania State University, University Park, PA, and approved June 17, 2016 (received for review April 7, 2016)

Interactions between catalytically active metal particles and reactant gases depend strongly on the particle size, particularly in the subnanometer regime where the addition of just one atom can induce substantial changes in stability, morphology, and reactivity. Here, time-lapse scanning tunneling microscopy (STM) and density functional theory (DFT)-based calculations are used to study how CO exposure affects the stability of Pt adatoms and subnano clusters at the Fe_3O_4(001) surface, a model CO oxidation catalyst. The results reveal that CO plays a dual role: first, it induces mobility among otherwise stable Pt adatoms through the formation of Pt carbonyls (Pt_1–CO), leading to agglomeration into subnano clusters. Second, the presence of the CO stabilizes the smallest clusters against decay at room temperature, significantly modifying the growth kinetics. At elevated temperatures, CO desorption results in a partial redispersion and recovery of the Pt adatom phase.

single-atom catalysis | adsorbate induced sintering | redispersion | Fe_3O_4 | nucleation and growth

Subnanometer metal particles exhibit a range of interesting electronic or catalytic properties that can vary substantially with the removal or addition of a single atom (1–6). Understanding the mechanistic details underlying the rearrangement of the active phase is important because changes in cluster size and shape are known to be commonplace under the conditions used in heterogeneous catalysis (7, 8), and because such processes are associated with deactivation phenomena such as sintering. Although sintering is usually regarded as a thermally activated process, there is increasing evidence that adsorbates influence sintering rates in a reactive environment by formation of mobile metal-molecule intermediates (2, 8–30). Indeed, in a previous study we demonstrated that the formation of highly mobile Pd_1–CO species led to enhanced sintering in the Pd/Fe_3O_4(001) system (31). Here, we turn our attention to Pt. Mobility is induced in the form of Pt_1–CO. In addition, CO stabilizes the smallest clusters. When it desorbs, Pt dimers break up into single atoms; thus, the CO is necessary for preserving nuclei that act as seeds for further growth. Using room-temperature scanning tunneling microscopy (STM), complemented by X-ray photoelectron spectroscopy (XPS) and density functional theory with an on-site Hubbard U (DFT+U), we follow the CO-induced diffusion and coalescence of Pt atom-by-atom, creating catalytically active (32) subnano clusters with a well-defined size distribution. On heating, desorption of CO leads to significant redispersion of Pt into the adatom phase.

Results

Fe_3O_4(001) is one of the most stable facets of magnetite (Fe_3O_4), a spinel-type ferrimagnetic conductive oxide (33) frequently used as a catalyst support. The surface exhibits a $(\sqrt{2}\times\sqrt{2})R45°$ reconstruction based on an ordered array of subsurface Fe vacancies and interstitials (34), which stabilizes metal adatoms [e.g., Au, Ag, and Pd (31, 35, 36)] in one specific site per unit cell against thermal sintering to temperatures as high as 700 K. Fig. 1*A* shows an STM image of the Fe_3O_4(001) surface following deposition of 0.2 ML Pt (1 ML = 1 adatom per reconstructed unit cell = 1.42×10^{14} atoms per cm^2). The characteristic undulating rows of the reconstructed Fe_3O_4(001) substrate are indicated by dark-blue lines (34). There are no O-related states in the vicinity of the Fermi energy (E_F); thus oxygen atoms, although present in the surface layer, are not imaged with the scanning conditions used here. Surface hydroxyl groups (O_SH), a common adsorbate at this surface after ultrahigh vacuum (UHV) preparation, are observed as a pair of extra-bright Fe atoms (cyan arrow) (37, 38). The Pt adatoms adsorb in two distinct configurations. First, protrusions located midway between the surface Fe rows indicate Pt twofold-coordinated to oxygen (Pt_1, Fig. 1*B*), the configuration commonly observed for other metal adatoms at this surface (31, 35, 36, 39, 40). DFT+U calculations find an adsorption energy $\Delta E_{ads}(Pt_1)$ of 3.89 eV compared with free Pt atoms in vacuum and little charge transfer to the surface (<0.5 e^-). A second configuration, labeled Pt_1*, not previously observed for other metals, appears offset to one side in STM images. Our DFT+U calculations find a stable adsorption site [$\Delta E_{ads}(Pt_1{}^*) = 3.01$ eV, charge transfer <0.3 e^-] bridging two oxygen atoms parallel to the rows of surface Fe (Fig. 1*C*). The Pt atom is observed to switch between these two configurations in STM image sequences collected in UHV conditions at room temperature (Fig. S1). The transition from $Pt_1{}^*$ to the Pt_1 state is strongly preferred, consistent with the higher binding energy of Pt_1 obtained in DFT+U calculations. Considering the large energy difference between the two adsorption sites, the high density of $Pt_1{}^*$ can only be explained by a large diffusion barrier between the sites. In DFT+U calculations, the energy barrier along an optimized diffusion path is found to be of the order of $\Delta E_{barr}(Pt_1{}^* \rightarrow Pt_1) \geq 0.9$ eV. Assuming an Arrhenius-type behavior, this energy results in a slow, thermally activated

Significance

The catalytic activity of metal particles is highly size-dependent in the subnanometer regime, which makes understanding how and why particle sizes change in reactive atmospheres particularly important. Here, we show that carbon monoxide plays a dual role in the coarsening of otherwise highly stable Pt atoms on an Fe_3O_4(001) support: CO adsorption weakens the adatom–support interaction inducing mobility, and stabilizes the Pt dimer against decay into two adatoms. Our results illustrate how molecules modify the clustering dynamics on surfaces, provide much-needed insight into how deactivation and redispersion can occur in single-atom catalyst systems, and demonstrate an approach to prepare size-distinguished clusters for studies of the size effect.

Author contributions: R.B., M.S., P.B., U.D., and G.S.P. designed research; R.B., J.E.S.v.d.H., J.H., J.P., and O.G. performed research; J.P., O.G., and P.B. contributed new reagents/analytic tools; R.B., J.E.S.v.d.H., J.H., P.E.d.J., M.S., P.B., and G.S.P. analyzed data; and R.B., M.S., U.D., and G.S.P. wrote the paper.

The authors declare no conflict of interest.

This article is a PNAS Direct Submission.

Freely available online through the PNAS open access option.

[1]To whom correspondence should be addressed. Email: parkinson@iap.tuwien.ac.at.

This article contains supporting information online at www.pnas.org/lookup/suppl/doi:10.1073/pnas.1605649113/-/DCSupplemental.

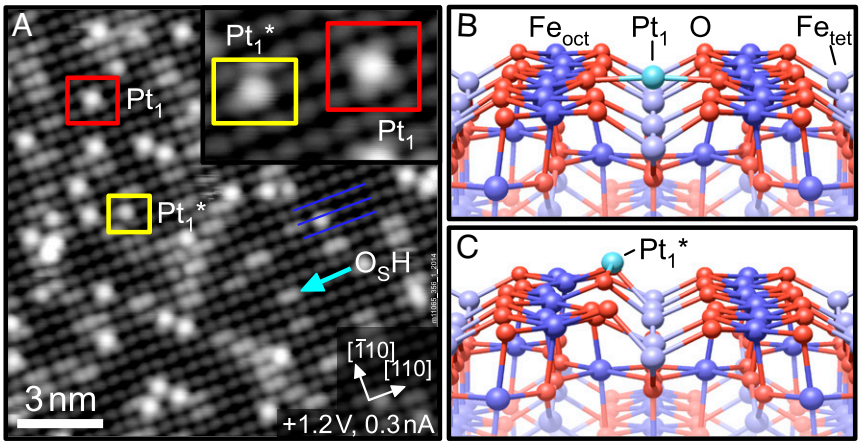

Fig. 1. (*A*) STM image of 0.2 ML Pt/Fe_3O_4 (001). The surface Fe_{oct} atoms are imaged as rows along the [110] direction (illustrated by the parallel blue lines). The bright features on the rows of Fe (example highlighted by cyan arrow) are due to surface OH groups (37, 38). The red and yellow frames highlight Pt adatoms in two different geometries: bridging surface O atoms in between (Pt_1) and parallel to (Pt_1*) the Fe_{oct} rows. (*B* and *C*) DFT+U-based force-relaxed structural models of the two adsorption configurations.

process at room temperature (of the order of $10^{-3}{\cdot}s^{-1}$ for an excitation frequency of 10^{13} s^{-1}). Annealing to 280 °C in UHV reduces the coverage of Pt_1* drastically, allowing the conclusion that the transition is thermally induced and the remaining Pt_1* features are likely stabilized by surface defects.

In Fig. 2, we show that CO adsorption on Pt_1 adatoms presents a clear signature in STM that can be interpreted with the aid of DFT+U calculations. Fig. 2 *A–D* shows a sequence of STM images acquired while exposing 0.15 ML Pt adatoms to 2×10^{-10} mbar CO. Fig. 2*A*, acquired before CO exposure ($P < 10^{-10}$ mbar), contains several Pt_1 and Pt_1* adatoms and a bright, double-lobed feature in the center of the scanning area. Increasing the CO pressure to 2×10^{-10} mbar (Fig. 2*B*) results in a second double-lobed feature at the former position of a Pt_1 adatom (labeled Pt_1–CO), and a new, single-lobed feature at the former position of a Pt_1* adatom (labeled Pt_1*–CO). Between Fig. 2 *B* and *D*, transitions between the Pt_1*–CO and Pt_1–CO state occur. Likely, both entities are chemically identical, i.e., they consist of one Pt atom and one CO molecule. The only difference between these species would be their adsorption geometry. To check whether adsorption of another molecule from the residual gas could be responsible for the observed features, we also exposed the as-deposited Pt adatoms to the most common components of the residual gas as measured by a quadrupole mass spectrometer: H_2, CO_2, CO, CH_4, H_2O, and O_2. (The presence of trace amounts of O_2 in our vacuum system is linked to the use of this gas during sample preparation.) No bond formation or other interactions with the Pt adatoms were observed for any gas molecule other than CO at room temperature.

DFT+U calculations for CO adsorption on Pt_1 adatoms are consistent with strong Pt–CO binding. The configuration of Pt_1–CO shown in Fig. 2*E* is favored by 5.53 eV compared with a free

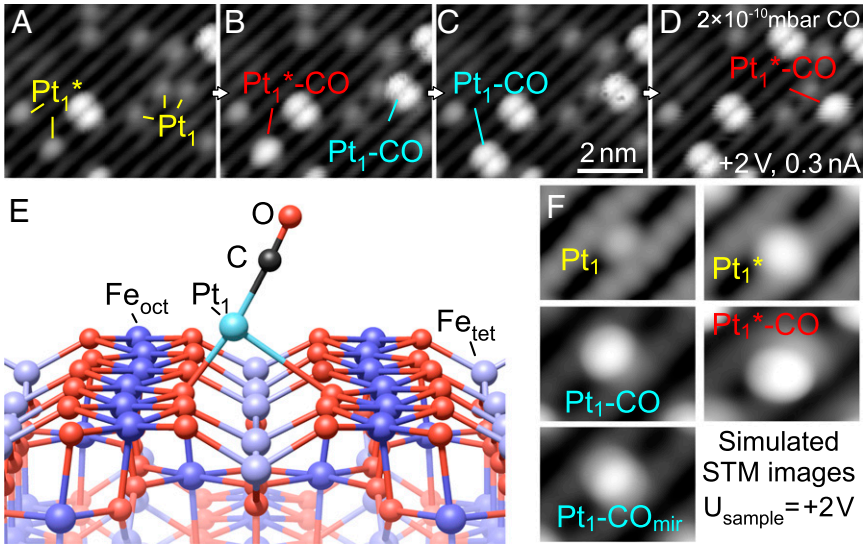

Fig. 2. CO adsorption and Pt site interchange. (*A–D*) STM image sequence (same place) acquired during exposure to 2×10^{-10} mbar CO. (*A*) Pt adatoms in two configurations (Pt_1, Pt_1*) and bright, double-lobed features are observed. (*B*) CO adsorption on Pt_1 and Pt_1 * adatoms results in bright, double-lobed and oval features, respectively. (*C*) The Pt_1*–CO labeled in red in *B* changes site, transforming into a Pt_1–CO feature. (*D*) The Pt_1–CO formed and labeled in cyan in *B* transforms into a Pt_1 *–CO feature. (*E*) Structural model of Pt_1–CO/Fe_3O_4(001). Upon adsorption of CO, the Pt adatom is lifted up and shifts perpendicular to the Fe rows to an off-centered position. (*F*) Simulated STM images at +2-V sample bias: Pt adatom, Pt* adatom, Pt_1–CO, mirrored Pt_1–CO. The latter is an overlay image of Pt_1–CO in the two equivalent off-centered positions to simulate switching during the scan, induced thermally or by the STM tip.

Pt atom and a free CO molecule in vacuum. The Pt_1 adatom is lifted up by ~1.3 Å away from the surface plane, and shifted perpendicular to the surface Fe-row direction. In this asymmetric geometry, one Pt–O bond is stretched to ~2.98 Å, which compares to ~2.03 Å for the second Pt–O bond and ~1.98 Å for both Pt–O bonds before CO adsorption. In STM images at 78 K (Fig. S2) and in simulated STM images (Fig. 2*F*) the Pt_1 carbonyl is imaged as a single, bright, oval protrusion, offset from the center of the Pt adsorption site. This resembles one of the two lobes observed in experiment. When this feature is scanned with a sample bias of +2 V (Fig. S2*C*), the protrusion switches repeatedly from one side of the unit cell to the other, suggesting that the STM tip can move the Pt–CO between two nearby sites that are energetically and symmetrically equivalent. Similar tip-induced switching behavior has been observed for dangling bond pairs on hydrogenated semiconductor surfaces (41, 42). To estimate the switching barrier we calculated the DFT energy of the likely transition state, a Pt_1–CO species centered between the Fe_{oct} rows. We found this energy to be only ~0.25 eV higher than the minima, suggesting that the double-lobed feature observed at room temperature is a time average of thermally activated switching. The Pt_1* adatom is also lifted up from the surface (by ~0.7 Å) by CO adsorption, but remains in the same location laterally. We considered the possibility that the double-lobed feature could be a Pt_1–$(CO)_2$ species. However, we never observed a different type of CO adsorption event, which would lead to Pt_1–CO in this case, although it should be clearly visible in STM. Moreover, the observed switching between the Pt_1*–CO and Pt_1–CO states agrees well with the energies derived from the DFT+U calculations.

Fig. 3 shows STM images of $Pt/Fe_3O_4(001)$ in a constant CO pressure of 2×10^{-10} mbar, selected from a 55-frame movie acquired over approximately 3 h. The CO induces mobility, and Pt clusters are formed over time. The sizes of the individual clusters are determined by tracking each individual Pt atom. Fig. 3*A* shows a large-area image of the surface after 10 min of CO exposure. The yellow frame highlights a smaller region selected for detailed analysis in Fig. 3 *B*–*G*. In Fig. 3*B*, four Pt adatoms are observed, two in Pt_1 configuration and two in Pt_1* configuration. Going through the panels from left to right we find that CO adsorbs initially on one Pt_1 and one Pt_1* (Fig. 3*C*), and that the Pt_1–CO feature then coalesces with the remaining Pt_1* adatom to form a Pt dimer in Fig. 3*D*. The Pt_1*–CO subsequently joins the dimer to form a trimer in Fig. 3*E*. Finally, the remaining Pt_1 adatom adsorbs a CO molecule in Fig. 3*F*, and coalesces with the trimer to form a Pt tetramer in Fig. 3*G*. It should be emphasized that, because of tip convolution effects, the identification of cluster sizes by their appearance is very hard if not impossible with STM (43). With our approach, the STM signature of the different cluster sizes can be ascertained, which allows determining the exact number of Pt atoms contained within each cluster in the larger scanned area (Fig. 3*H*). In Fig. 3 the largest clusters contain four atoms. The cluster size distribution in areas scanned with the STM during the CO exposure is comparable to those in areas located further away. Thus, the Pt_1–CO mobility and sintering is not induced by the STM tip.

It is important to note that the Pt carbonyl is the only diffusing species observed in the STM movies. Dimers, trimers, and larger clusters are immobile, even in CO pressures up to 10^{-6} mbar. Fig. 4*A* shows an STM image of 0.15 ML $Pt/Fe_3O_4(001)$ acquired as part of a different STM movie starting from adatoms where the CO pressure was increased up to 10^{-6} mbar in a stepwise manner. As in Fig. 3, we determine the number of Pt atoms in each cluster by watching its assembly. The resulting size distribution is narrow, ranging from one to five atoms. The majority of clusters contain two or three atoms. The bar graph illustrates the number density of Pt clusters (blue, 71.5 ± 4.7% of all features, 5.69×10^{16} clusters per m^2) versus the adatom phase (yellow,

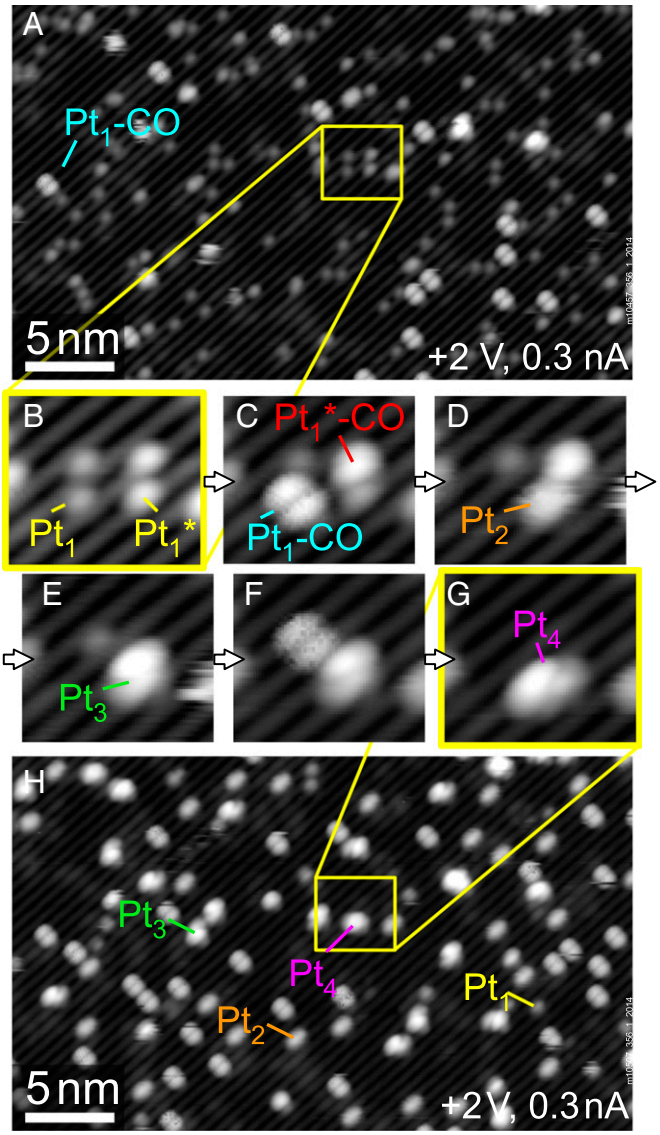

Fig. 3. CO-induced Pt diffusion and coalescence. STM image sequence acquired during exposure to 2×10^{-10} mbar CO. (*A*) After 5 h in UHV and 10 min CO exposure: Pt adatoms coexist with a few double-lobed, bright features, identified as Pt_1–CO created by CO adsorption in Fig. 2. (*B*–*G*) Formation of a Pt tetramer: CO adsorption on Pt_1 and Pt_1*, mobility, and coalescence are observed atom by atom. (*H*) Partially sintered state: Only a few adatoms remain; the biggest clusters in this image contain four atoms.

2.27×10^{16} adatoms per m^2). The graph represents the average from two experiments in which 0.15 ML Pt adatoms were sintered in different amounts of CO. In both cases the remaining adatom density was between 0.01 and 0.02 ML. The shaded area corresponds to the respective standard deviation.

To investigate the stability of the subnano clusters formed by CO-induced sintering at reaction temperatures, we heated the surface to 520 K in UHV. The average coverage of Pt adatoms increased by almost 130%, and the number of clusters decreased by more than 60%. The remaining clusters were larger, with an average size of ~7.6 atoms (~3.3 atoms before annealing). This trend is again illustrated by the bar graph beneath the STM image in Fig. 4*B*, which clearly shows that adatoms are the dominant Pt-related feature after annealing (71.2 ± 8.9%). The complete absence of small clusters suggests that these species are unstable without CO, and that CO desorption drives the breakup. In a control experiment, the

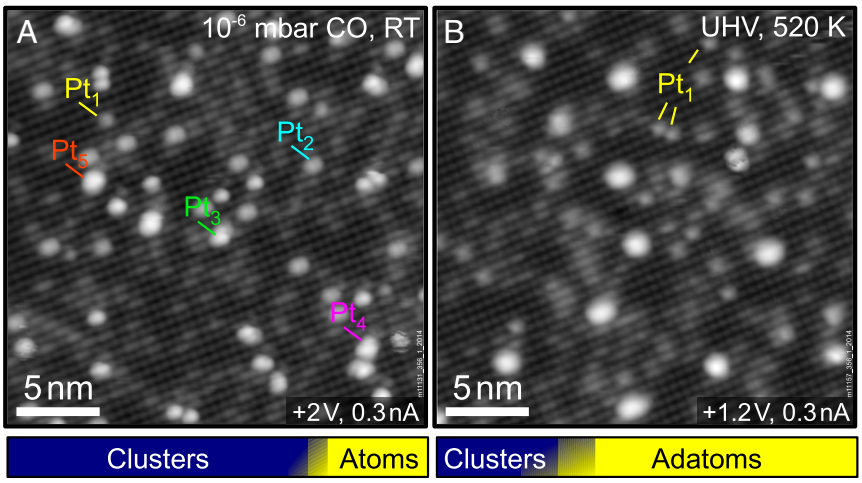

Fig. 4. Sintering at high CO pressure and redispersion of small clusters by annealing. The bar graphs at the bottom show the average adatom and cluster density in each case. (*A*) $Pt/Fe_3O_4(001)$ after exposure to CO pressures up to 10^{-6} mbar. The main features are small clusters (Pt_2, Pt_3); the largest observed clusters consist of five atoms. (*B*) A different region of the sample after annealing to 520 K in UHV. Interestingly, more adatoms are now present at the surface. The number of clusters has decreased and the average cluster size is considerably larger.

adatoms were heated in UHV without prior exposure to CO. This treatment leads to a small decrease in the adatom density, but no discernible change in the cluster density. This suggests that the adatoms become mobile at 520 K and can incorporate within existing clusters. Crucially, the constant cluster density highlights the importance of CO for new cluster nucleation. The crucial role of CO for the stability of the clusters is supported by the XPS measurements in Fig. 5, which show that CO was adsorbed on the clusters following room-temperature exposure, but desorbs after heating to 520 K. Before CO exposure (blue curves) the Pt $4f_{7/2}$ peak at 71.4 eV resembles that of metallic Pt, consistent with the very small electron transfer predicted by DFT+U. Following 120 L CO exposure (red) a peak appears in the C 1*s* region at 287.7 eV, which is higher than CO adsorbed in an atop site on Pt(111) (286.8 eV). The adsorption of the CO causes the Pt 4*f* to shift up in binding energy to 72.4 eV, which is also higher than when CO is adsorbed atop on Pt(111). Finally, heating above the desorption temperature of CO on Pt (~500 K), the peak in C1*s* is gone and the Pt 4*f* peak shifts back to the metallic position. Note that CO does not adsorb on the pristine $Fe_3O_4(001)$ surface at room temperature, where all experiments were performed.

The assertion that Pt cluster stability is linked to adsorbed CO is supported by DFT+U calculations. In the absence of CO, two Pt_1 isolated adatoms are preferred to a Pt dimer (two adatoms: 7.78 eV, one Pt dimer: 6.35 eV with respect to Pt in the gas phase). A $Pt_2(CO)_1$ species is also unfavorable with respect to one Pt_1 carbonyl and one adatom ($E[Pt_2(CO)] = 8.44$ eV and $E[Pt_1 + Pt_1CO] = 3.89$ eV + 5.53 eV = 9.42 eV). Crucially, a Pt dimer with two adsorbed CO molecules is slightly more stable than two Pt_1–CO species (11.16 eV compared with 11.06 eV). Thus, the formation of dimers can only proceed in the presence of (at least) two adsorbed CO molecules. When CO is desorbed, the strong Pt_1/Fe_3O_4 interaction leads to a redispersion of Pt, and a partial recovery of the adatom phase.

Discussion

The agglomeration phenomena described here are a clear case of gas-induced coarsening, a well-known process that causes

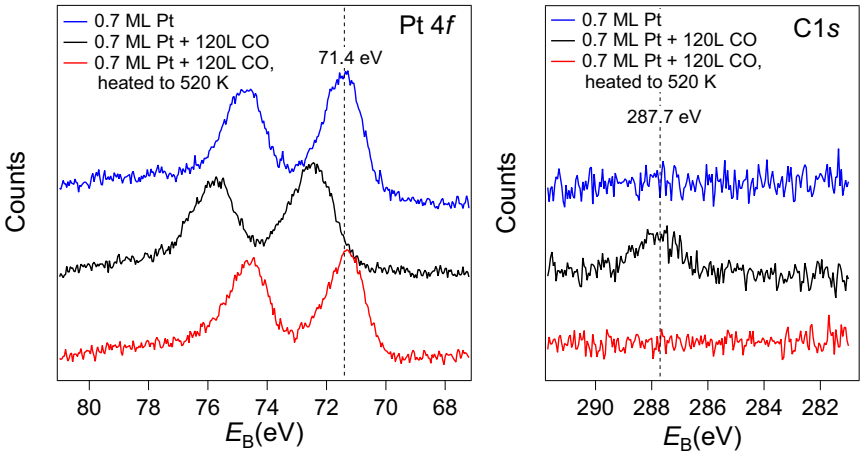

Fig. 5. XPS spectra of the Pt 4*f* and C 1*s* regions acquired after the deposition of 0.7 ML Pt (blue), after CO exposure (20 min, 10^{-7} torr, black), and after annealing to 520 K (red). After deposition Pt adatoms are the main species, coexisting with a small number of clusters and Pt carbonyls formed by adsorption from the background gas. After CO exposure all Pt adatoms have adsorbed CO and coalesced to small clusters. Annealing to 520 K causes the CO to desorb. The Pt peak shifts back to an energy slightly lower than its initial position, indicating the complete absence of CO and the coexistence of adatoms and clusters.

catalyst deactivation. Nevertheless, unequivocal identification of the mobile species is rare, and through our combined use of STM, XPS, and DFT, we clearly demonstrate that a Pt_1–CO species drives the coalescence of single Pt atoms into clusters. Moreover, we demonstrate this occurs because the adsorption of the CO molecule weakens the Pt–O bonds, facilitating diffusion. Adsorption of one CO (which, as argued above, appears as a double-lobed feature in STM) is sufficient to allow the Pt to move across the surface.

In recent years knowledge of the size effect in subnano catalysis has been revolutionized by the ability to deposit size-selected clusters on model support surfaces (6, 44–47). Our approach to monitor cluster formation in an atom-by-atom fashion produces a model system where the cluster size and distribution is accurately known. Following the behavior of such "size-distinguished" ensembles in reactive atmospheres could provide valuable insights into catalytic reactions in the nonscalable cluster regime. Indeed, we recently demonstrated that subnano Pt clusters grown by the CO-induced sintering approach are active for CO and H_2 oxidation via a Mars–van Krevelen-type mechanism (32).

Surprisingly, we find that the CO also stabilizes dimers against decay. Thus, in addition to providing mobility, CO plays a crucial role in the growth kinetics by providing stability to the smallest clusters that act as further nucleation sites. In the UHV environment, the binding of the metal adatoms to the substrate is sufficiently strong that spontaneous formation of a Pt dimer is energetically unfavorable. Similar behavior was observed previously for Ag on the same surface, and extremely high adatom coverages were achieved because the nucleation of stable clusters was suppressed (35, 36). Here, this limitation is bypassed when two Pt_1–CO species meet, because their merger produces a $Pt_2(CO)_2$ dimer that is stable and can function as a seed for further growth. When the sample is heated, the CO desorbs, and the small clusters break up into single Pt atoms.

The results described here contain several important lessons for the rapidly emerging, yet controversial field of single-atom catalysis. Here, the goal is to use single atoms as active sites for catalytic reactions to maximize the efficient use of noble metals such as Pt. Sintering clearly runs counter to this objective, and the ability to rapidly recover the adatom phase is considered vital to economic viability. In our work, the strong CO–Pt_1 interaction is clearly detrimental as it accelerates the sintering process. The problem of the strong CO–Pt_1 bond has been recognized before, and has been proposed to poison low-temperature oxidation reactions on a variety of substrates (48). Based on our results, it seems plausible that the catalytic activity reported for single-atom catalysts based on Pt could result from subnano particles formed under reaction conditions, which subsequently redisperse after the fact. In this light, although Pt is clearly an excellent catalyst as a nanoparticle, a less reactive (cheaper) metal would almost certainly yield a better and more stable single-atom catalyst. It would be fascinating indeed if, in an attempt to reduce the amount of Pt, it becomes possible to circumvent its use entirely.

In summary, we have analyzed the interaction of CO with Pt adatoms and clusters in detail. CO-induced mobility leads to the agglomeration of Pt into subnano clusters, and the presence of the CO stabilizes the smallest clusters against decay. Our results provide insights into coarsening processes at surfaces, which should be applicable to established catalysts based on oxide-supported metal clusters. CO-induced adatom sintering provides a well-defined initial state for experiments into the size-dependent properties of small Pt clusters.

Experimental Methods

The STM experiments were performed in a two-vessel UHV system. It consists of a preparation chamber and an analysis chamber. The latter is equipped with an Omicron μ-STM, which was operated in constant current mode. The substrate material was a synthetic Fe_3O_4(001) crystal grown using the floating zone method (49). The crystal was prepared by cycles of sputtering with Ar^+ ions (E_{Ar} = 1 keV, j_{sample} = 6.5 μA/cm^2, 10 min) followed by annealing at 870 K in 6.6 × 10^{-7} mbar O_2 (15 min). Temperatures were measured with a K-type thermocouple attached to the sample holder. The systematic error of the measurement is estimated as ±20 K (at 520 K). At high temperatures, the uncertainty of the temperature readout increases (±50 K at 900 K) because the thermocouple is not attached directly to the sample. The XPS data were acquired in a second UHV chamber equipped with a He-flow cryostat, a twin-anode X-ray source (Al, Ag), a Focus 500 monochromator, and a SPECS Phoibos 150 analyzer. In this system, the sample is prepared by cycles of sputtering with Ne^+ ions (E_{Ne} = 1 keV, j_{sample} ~ 2.3 μA/cm^2) and annealing in O_2 using a directional doser creating a local pressure of $P = 10^{-6}$ mbar at the sample. In both chambers Pt was deposited using a modified Omicron single-pocket electron-beam evaporator. The deposition rate (~0.3 ML/min, 1 ML = 1 atom per reconstructed unit cell = 1.42 × 10^{18} m^{-2}) was calibrated using a water-cooled quartz-crystal microbalance.

The DFT calculations are based on the augmented plane wave + local orbital method as implemented in Wien2K (50). We used the generalized gradient approximation with a Hubbard U (U_{eff} = 3.8 eV) to treat the strongly correlated Fe 3*d* electrons. The adsorption of Pt adatoms was modeled on a 17-layer 2 × 2 supercell of the $\sqrt{2}\times\sqrt{2}$-reconstructed Fe_3O_4(001) surface with inversion symmetry and a vacuum layer of ~13 Å. In total, the slab contains 244 atoms plus 2 or 4 Pt atoms and 2 or 4 C and O atoms in the calculations including CO molecules. The atomic sphere sizes used for Fe, O, and Pt were 0.98, 0.79, and 1.11 Å, respectively. A plane-wave cutoff of RK_{max} = 7.0 corresponding to 296.6 eV was used, and the Brillouin zones of the surface models were sampled with a 3- × 3- × 1-*k* mesh. The surface models were relaxed until all forces were below 1 mRy/bohr (26 meV/Å). A Fermi broadening of 0.08 eV was used. The charge transfer from Pt adatoms to the slab was estimated from the change in the partial charge distribution in the Pt atom and the change in the magnetic moment of the total slab, the Pt adatom, and the adjacent O atoms.

ACKNOWLEDGMENTS. G.S.P., R.B., O.G., J.H., and J.P. acknowledge funding from the Austrian Science Fund (FWF) START Prize Y 847-N20 and Project P24925-N20. R.B. and O.G. acknowledge a stipend from the Vienna University of Technology and the FWF as part of the doctoral college SOLIDS4FUN (W1243). P.E.d.J. acknowledges support from NWO-Vici 724.012.001. U.D. and J.P. acknowledge support by the European Research Council (Advanced Grant "OxideSurfaces"). M.S. was supported by the FWF within SFB F45 "FOXSI." P.B. was supported by the FWF (Projects SFB F41 "ViCoM" and the doctoral college W1243 "Solids4Fun").

1. Heiz U, Sanchez A, Abbet S, Schneider WD (1999) Catalytic oxidation of carbon monoxide on monodispersed platinum clusters: Each atom counts. *J Am Chem Soc* 121(13):3214–3217.
2. Bonanni S, Aït-Mansour K, Harbich W, Brune H (2014) Reaction-induced cluster ripening and initial size-dependent reaction rates for CO oxidation on $Pt_{(n)}/TiO_2$(110)-(1×1). *J Am Chem Soc* 136(24):8702–8707.
3. Lee S, Fan C, Wu T, Anderson SL (2005) Cluster size effects on CO oxidation activity, adsorbate affinity, and temporal behavior of model $Au_{(n)}/TiO_2$ catalysts. *J Chem Phys* 123(12):124710.
4. Zhou X, et al. (2016) Stable Pt single atoms and nanoclusters on ultrathin CuO film and their performances in CO oxidation. *J Phys Chem C* 120(3):1709–1715.
5. Turner M, et al. (2008) Selective oxidation with dioxygen by gold nanoparticle catalysts derived from 55-atom clusters. *Nature* 454(7207):981–983.
6. Tyo EC, Vajda S (2015) Catalysis by clusters with precise numbers of atoms. *Nat Nanotechnol* 10(7):577–588.
7. Fukamori Y, et al. (2013) Fundamental insight into the substrate-dependent ripening of monodisperse clusters. *ChemCatChem* 5(11):3330–3341.
8. Newton MA, Belver-Coldeira C, Martínez-Arias A, Fernández-García M (2007) Dynamic in situ observation of rapid size and shape change of supported Pd nanoparticles during CO/NO cycling. *Nat Mater* 6(7):528–532.
9. Kellogg GL (1997) Hydrogen promotion of surface self-diffusion on Rh(100) and Rh(311). *Phys Rev B* 55(11):7206–7212.
10. Horch S, et al. (1999) Enhancement of surface self-diffusion of platinum atoms by adsorbed hydrogen. *Nature* 398(6723):134–136.
11. Feibelman PJ (2000) Formation and diffusion of S-decorated Cu clusters on Cu(111). *Phys Rev Lett* 85(3):606–609.
12. Ling WL, et al. (2004) Enhanced self-diffusion on Cu(111) by trace amounts of S: Chemical-reaction-limited kinetics. *Phys Rev Lett* 93(16):166101.
13. Layson AR, Thiel PA (2001) Testing realistic environments for metal film growth and aging: Chemical insights into the effect of oxygen on Ag/Ag(100). *Surf Sci* 472(3): L151–L156.
14. Layson AR, Evans JW, Thiel PA (2002) Additive-enhanced coarsening and smoothening of metal films: Complex mass-flow dynamics underlying nanostructure evolution. *Phys Rev B* 65(19):193409.

15. Starr DE, Shaikhutdinov SK, Freund H-J (2005) Gold supported on oxide surfaces: Environmental effects as studied by STM. *Top Catal* 36(1-4):33–41.
16. Kibsgaard J, Morgenstern K, Laegsgaard E, Lauritsen JV, Besenbacher F (2008) Restructuring of cobalt nanoparticles induced by formation and diffusion of monodisperse metal-sulfur complexes. *Phys Rev Lett* 100(11):116104.
17. Thiel PA, Shen M, Liu D-J, Evans JW (2010) Adsorbate-enhanced transport of metals on metal surfaces: Oxygen and sulfur on coinage metals. *J Vac Sci Technol A* 28(6):1285–1298.
18. Akdogan Y, et al. (2009) Reconstruction of Pt_{13} clusters into $Pt_2(CO)_m$ on CO addition in NaY zeolite. *J Phys Chem C* 113(6):2352–2359.
19. Thiel PA, Shen M, Liu D-J, Evans JW (2009) Coarsening of two-dimensional nanoclusters on metal surfaces. *J Phys Chem C* 113(13):5047–5067.
20. Khajetoorians AA, et al. (2009) Adsorbate-induced restructuring of Pb mesas grown on vicinal Si(111) in the quantum regime. *Phys Rev B* 80(24):245426.
21. Simonsen SB, et al. (2010) Direct observations of oxygen-induced platinum nanoparticle ripening studied by in situ TEM. *J Am Chem Soc* 132(23):7968–7975.
22. Brown MA, et al. (2011) Oxidation of Au by surface OH: Nucleation and electronic structure of gold on hydroxylated MgO(001). *J Am Chem Soc* 133(27):10668–10676.
23. Chaâbane N, Lazzari R, Jupille J, Renaud G, Avellar Soares E (2012) CO-induced scavenging of supported Pt nanoclusters: A GISAXS study. *J Phys Chem C* 116(44):23362–23370.
24. Gerber T, et al. (2013) CO-induced Smoluchowski ripening of Pt cluster arrays on the graphene/Ir(111) moiré. *ACS Nano* 7(3):2020–2031.
25. Sehested J, Larsen NW, Falsig H, Hinnemann B (2014) Sintering of nickel steam reforming catalysts: Effective mass diffusion constant for Ni-OH at nickel surfaces. *Catal Today* 228:22–31.
26. Jiang P, Bao X, Salmeron M (2015) Catalytic reaction processes revealed by scanning probe microscopy. [corrected]. *Acc Chem Res* 48(5):1524–1531.
27. Walen H, et al. (2015) Cu_2S_3 complex on Cu(111) as a candidate for mass transport enhancement. *Phys Rev B* 91(4):045426.
28. Ouyang R, Liu J-X, Li W-X (2013) Atomistic theory of Ostwald ripening and disintegration of supported metal particles under reaction conditions. *J Am Chem Soc* 135(5):1760–1771.
29. Kistamurthy D, Saib AM, Moodley DJ, Niemantsverdriet JW, Weststrate CJ (2015) Ostwald ripening on a planar Co/SiO_2 catalyst exposed to model Fischer–Tropsch synthesis conditions. *J Catal* 328:123–129.
30. Harris PJF (1995) Growth and structure of supported metal catalyst particles. *Int Mater Rev* 40(3):97–115.
31. Parkinson GS, et al. (2013) Carbon monoxide-induced adatom sintering in a Pd-Fe_3O_4 model catalyst. *Nat Mater* 12(8):724–728.
32. Bliem R, et al. (2015) An atomic-scale view of CO and H_2 oxidation on a Pt/Fe_3 O_4 model catalyst. *Angew Chem Int Ed Engl* 54(47):13999–14002.
33. Cornell RM, Schwertmann U (2003) *The Iron Oxides: Structure, Properties, Reactions, Occurrences and Uses* (Wiley-VCH, Weinheim, Germany).
34. Bliem R, et al. (2014) Subsurface cation vacancy stabilization of the magnetite (001) surface. *Science* 346(6214):1215–1218.
35. Novotný Z, et al. (2012) Ordered array of single adatoms with remarkable thermal stability: Au/Fe_3O_4(001). *Phys Rev Lett* 108(21):216103.
36. Bliem R, et al. (2014) Cluster nucleation and growth from a highly supersaturated adatom phase: Silver on magnetite. *ACS Nano* 8(7):7531–7537.
37. Parkinson GS, Novotný Z, Jacobson P, Schmid M, Diebold U (2011) Room temperature water splitting at the surface of magnetite. *J Am Chem Soc* 133(32): 12650–12655.
38. Parkinson GS, et al. (2010) Semiconductor-half metal transition at the Fe_3O_4(001) surface upon hydrogen adsorption. *Phys Rev B* 82(12):125413.
39. Parkinson GS, Novotny Z, Jacobson P, Schmid M, Diebold U (2011) A metastable Fe(A) termination at the Fe_3O_4(001) surface. *Surf Sci Lett* 605(15):L42.
40. Bliem R, et al. (2015) Adsorption and incorporation of transition metals at the magnetite Fe_3O_4(001) surface. *Phys Rev B* 92(7):075440.
41. Engelund M, et al. (2015) Tunneling spectroscopy of close-spaced dangling-bond pairs in Si(001):H. *Sci Rep* 5:14496.
42. Godlewski S, et al. (2015) Dynamical behavior of a dangling bond dimer on a hydrogenated semiconductor: Ge(001):H. *Phys Rev B* 92(11):115403.
43. Emmrich M, et al. (2015) Surface structure. Subatomic resolution force microscopy reveals internal structure and adsorption sites of small iron clusters. *Science* 348(6232):308–311.
44. Campbell CT, Parker SC, Starr DE (2002) The effect of size-dependent nanoparticle energetics on catalyst sintering. *Science* 298(5594):811–814.
45. Xu Z, et al. (1994) Size-dependent catalytic activity of supported metal clusters. *Nature* 372(6504):346–348.
46. Roldan Cuenya B, Behafarid F (2015) Nanocatalysis: Size- and shape-dependent chemisorption and catalytic reactivity. *Surf Sci Rep* 70(2):135–187.
47. Kaden WE, Wu T, Kunkel WA, Anderson SL (2009) Electronic structure controls reactivity of size-selected Pd clusters adsorbed on TiO_2 surfaces. *Science* 326(5954): 826–829.
48. Ding K, et al. (2015) Identification of active sites in CO oxidation and water-gas shift over supported Pt catalysts. *Science* 350(6257):189–192.
49. Mao ZQ, Maenoab Y, Fukazawa H (2000) Crystal growth of Sr_2RuO_4. *Mater Res Bull* 35(11):1813–1824.
50. Blaha P, Schwarz K, Madsen GKH, Kvasnicka D, Luitz J (2001) *WIEN2K, An Augmented Plane Wave + Local Orbitals Program for Calculating Crystal Properties* (Karlheinz Schwarz, Vienna University of Technology, Vienna).